

# Spectral entropy of the discrete Hasimoto effective potential exposes sub-residue geometric transitions in protein secondary structure

Yiquan Wang\*

*College of Mathematics and System Science, Xinjiang University, Urumqi, Xinjiang, China*

*Xinjiang Key Laboratory of Biological Resources and Genetic Engineering,*

*College of Life Science and Technology, Xinjiang University, Urumqi, Xinjiang, China and  
Shenzhen X-Institute, Shenzhen, China*

(Dated: February 26, 2026)

Characterizing the precise geometric boundaries of protein secondary structures is fundamental to understanding macromolecular folding and conformational dynamics. By applying the discrete Hasimoto map to translate three-dimensional backbone geometry into a one-dimensional discrete nonlinear Schrödinger effective potential  $V_{\text{re}}[n]$  we establish a rigorous frequency-domain framework for protein conformations. Systematic short-time Fourier transform analysis across 320,453 residues from 1,986 non-redundant proteins allows us to define a local spectral entropy  $H_{\text{spec}}$  that consistently orders structural states. Helical segments emerge as narrow-band low-entropy spectral regimes dominated by their zero-frequency components whereas coil fluctuations manifest as broadband noise. Crucially we demonstrate that the boundaries separating these states exhibit step-like sharpness characteristic of a first-order-like geometric transition with a sub-residue median width of 0.145 residues. This abrupt kinematic transition provides an independent spatial counterpart to the cooperative Zimm-Bragg thermodynamic model of helix nucleation. The extreme spatial narrowness of this boundary exposes an intrinsic limitation governed by the Gabor spatial-spectral uncertainty principle. This trade-off imposes a maximal-localization constraint that explains why the pointwise zero-window integrability residual  $E[n]$  acts as an effective high-pass filter for boundary detection. Guided by this physical limit we introduce a dual-probe approach combining the high-pass residual to capture local torsion discontinuities with a low-frequency energy ratio  $R_{\text{LF}}$  to measure the direct-current dominated flatness inherent to helical interiors. Unifying these complementary signals more comprehensively captures the geometric context and improves the detection area under the curve from 0.783 to 0.815. Because high-entropy broadband regions coincide with the conformationally flexible loops and hinges implicated in allostery, the spectral entropy of the Hasimoto potential may serve as a sequence-agnostic geometric proxy for mapping functional dynamics directly from backbone coordinates.

## I. INTRODUCTION

The geometry of a protein backbone encodes the full spectrum of information from local hydrogen-bond chemistry to macroscopic topological folding. At each sequential  $C_{\alpha}$  position  $n$ , the bond-angle curvature  $\kappa[n]$  and dihedral torsion  $\tau[n]$  fully characterize this three-dimensional space curve as a spatially evolving physical signal. In  $\alpha$ -helical segments, both quantities adopt nearly constant values dictated by regular hydrogen-bonding patterns; in coil and loop regions, they fluctuate widely. Precisely delineating the geometric boundaries between these secondary structure states is a prerequisite for understanding macromolecular folding, allostery, and conformational dynamics. This boundary problem is inherently interdisciplinary. Chemistry-based algorithms such as DSSP [1] and STRIDE [2] define structure through local atomic interactions and hydrogen-bond energetics, providing foundational but discrete assignments that lack a continuous-medium dynamical description [3]. Geometry-only methods such as P-SEA [4] assign structure directly from the  $C_{\alpha}$  trace, yet remain purely rule-based, and more recent graph-based approaches can operate without sequence information [5]. A rich physics tradition has modeled backbones using differential geometry [6, 7], conceptualizing folds as topological solitons via discrete Frenet frames [8–12] and echo-

ing early theories of nonlinear energy transfer along protein chains [13]. Sequence-based prediction methods achieve considerable success in assigning secondary structure from amino acid sequences alone [14], and end-to-end structure prediction networks now produce full three-dimensional models at near-experimental accuracy [15], yet these approaches operate on one-dimensional chemical or evolutionary information without explicitly exploiting the differential geometry of the backbone. Classical signal processing has likewise isolated protein periodicities [16–21], and spectral methods such as the Informational Spectrum Method and Resonant Recognition Model have mapped amino acid physicochemical properties, notably the Electron-Ion Interaction Potential derived from pseudopotential theory, into frequency-domain representations linked to biological function [22–24]; recent deep-learning approaches have further generalized this concept by transforming sequences into spectrogram representations [25]. However, these methods predominantly operate on one-dimensional scalar sequences rather than the true three-dimensional backbone geometry. Each of these traditions captures a distinct facet of protein structure, yet the underlying physical mechanisms that govern the sharpness and spatial extent of structural boundaries remain to be elucidated.

Elucidating these mechanisms requires a mathematical language capable of rigorously projecting three-dimensional backbone geometry into a one-dimensional physical field amenable to frequency-domain analysis. The discrete Hasimoto map, originating in vortex filament dynamics [26], provides a natural framework for this projection by combin-

\* ethan@stu.xju.edu.cn

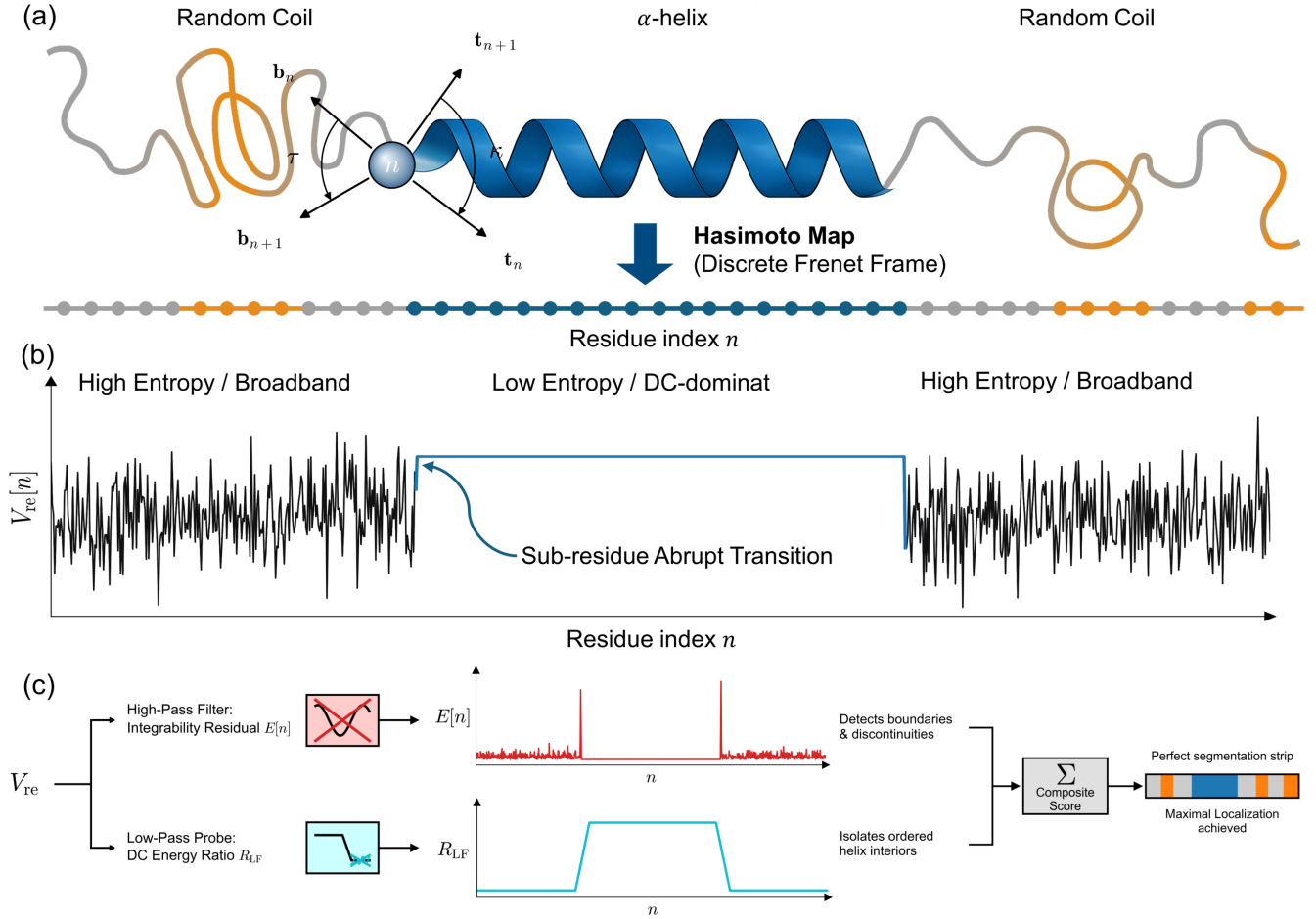


FIG. 1. Conceptual signal-processing framework for protein secondary structure detection via the discrete Hasimoto map. (a) Physical Mapping: The 3D geometry of the protein backbone (characterized by bond-angle curvature  $\kappa$  and torsion  $\tau$ ) is projected onto a 1D lattice via the discrete Frenet frame. (b) Signal Dichotomy: The Hasimoto effective potential  $V_{\text{re}}[n]$  translates structurally ordered states ( $\alpha$ -helices) into flat, negative DC plateaus denoting narrow-band, low-spectral-entropy regimes. Conversely, disordered loops (coils) manifest as large-amplitude broadband fluctuations. The boundaries between these states exhibit remarkably sharp, sub-residue step-like transitions. (c) Dual-Probe Filter Bank: Structural boundary detection is recast as a spectral filtering problem. The integrability residual  $E[n]$  acts as a pointwise high-pass filter, suppressing the helical interior while sensitively detecting boundary discontinuities (red spikes). Conversely, the low-frequency energy ratio  $R_{\text{LF}}$  explicitly isolates the flat DC core of the ordered helix. Combining these dual probes more comprehensively captures the geometric context under the maximal-localization constraint.

ing curvature and torsion into a complex scalar field  $\psi[n] = \kappa[n] \exp(i \sum_{k=1}^n \tau[k])$ . This field evolves according to a discrete nonlinear Schrödinger (DNLS) equation through an effective potential  $V_{\text{eff}}[n] = V_{\text{re}}[n] + iV_{\text{im}}[n]$  that encodes the deviation of the backbone from an ideal integrable curve. The real part  $V_{\text{re}}[n]$  admits an exact analytic decomposition [27]:

$$V_{\text{re}}[n] = \beta^+ r^+[n] \cos \tau[n+1] + \beta^- r^-[n] \cos \tau[n] - (\beta^+ + \beta^-), \quad (1)$$

where  $r^\pm[n] = \kappa[n \pm 1] / \kappa[n]$  are nearest-neighbor curvature ratios and  $\beta^\pm$  are inverse bond lengths. Recent work established this map as a fundamental kinematic identity for proteins and defined an integrability residual,

$$E[n] = \left| \cos \tau[n] - \left( 1 + \frac{V_{\text{re}}[n]}{2\beta} \right) \right|, \quad (2)$$

to measure the departure of local geometry from the DNLS dispersion relation [27]. Subsequent research demonstrated that, under a uniform-curvature approximation,  $E[n]$  functions as a spatial high-pass filter capable of identifying piecewise integrable islands for highly accurate three-dimensional analytic reconstruction [28]. These spatial-domain results establish the Hasimoto potential as a physically grounded structural descriptor. In this study, we apply the short-time Fourier transform (STFT) directly to  $V_{\text{re}}[n]$ , transitioning from the spatial domain into the spatial-frequency domain to investigate the dynamic physical mechanisms that underlie these empirical successes.

In the spatial-frequency domain, protein secondary structures exhibit a clear physical dichotomy. Helical segments emerge as narrow-band, low-entropy frequency modes domi-

nated by their zero-frequency (DC) components, whereas coil regions distribute energy across the entire spectrum as broadband noise. The boundaries separating these two spectral regimes are remarkably sharp, exhibiting sub-residue transition widths consistent with an abrupt geometric transition and a directional asymmetry in which helix exits are sharper than helix entries.

This extreme spatial narrowness exposes an intrinsic constraint governed by the Gabor spatial-spectral uncertainty principle [29]: expanding the STFT observation window improves frequency resolution but inevitably blurs the sub-residue boundary. This trade-off establishes a maximal-localization constraint under which boundary detection accuracy is maximized at the narrowest feasible window, providing a physical rationale for the empirical observation that the pointwise, zero-window operator  $E[n]$  achieves the highest boundary detection accuracy among the descriptors tested [27, 28].

Guided by this physical duality, we construct a dual-probe signal-processing framework (Fig. 1). The discrete Hasimoto map first translates three-dimensional backbone geometry into a one-dimensional effective potential (Fig. 1a), mapping structurally ordered helices to flat DC plateaus and disordered coils to broadband noise (Fig. 1b). The pointwise integrability residual  $E[n]$  serves as a high-pass probe that captures torsion discontinuities at structural boundaries, while a newly introduced low-frequency energy ratio  $R_{LF}$  serves as a low-pass probe that measures the DC-dominated spectral flatness inherent to helical interiors (Fig. 1c). Combining these complementary probes reconciles local boundary precision with global topological robustness, substantially improving detection accuracy. By mapping three-dimensional structures into one-dimensional frequency spectra, this framework suggests that broadband, high-entropy geometries may correspond to the conformational flexibility associated with protein interactions and allostery, motivating future validation against experimental dynamics data.

## II. METHODS

We constructed two datasets from the RCSB Protein Data Bank [30]. The main dataset is derived from the CullPDB non-redundant list [31] (sequence identity  $\leq 25\%$ , resolution  $\leq 2.0$  Å, X-ray structures only, chain length 40–300 residues, downloaded February 2026), which provides 2004 unique chains. Each chain was subjected to the following quality filters: (i) at least 7  $C_\alpha$  atoms (the minimum required to produce at least one  $V_{re}$  value after Frenet-frame trimming); (ii) all  $C_\alpha$ – $C_\alpha$  virtual bond lengths within the range 1.0–10.0 Å (to exclude chains with missing residues or coordinate errors; the standard  $C_\alpha$ – $C_\alpha$  distance is approximately 3.8 Å); (iii) no vanishing bond-angle curvature ( $\kappa > 10^{-15}$  rad at every position, to avoid division by zero in the curvature ratios  $r^\pm$ ); and (iv) successful DSSP secondary structure calculation. After applying these filters, the final set comprises 1,986 chains (320,453 aligned residues), of which 852 overlap with the original 856-protein dataset of Ref. [27]. The helical

peptide dataset was assembled by selecting all main-dataset chains with DSSP helix fraction  $\geq 70\%$  and augmenting with the 50 high-helicity short peptides from Ref. [28] (20–50 residues, helix fraction  $> 85\%$ ; 49 of 50 passed the quality filters above), yielding 251 chains (mean helix fraction 83.4%, length range 22–298). Table I summarizes both datasets. Secondary structure labels were computed using DSSP (mkdssp) [1, 32], which identifies hydrogen bonds from backbone N–H and C=O electrostatic interaction energies (threshold  $< -0.5$  kcal/mol) and assigns one of eight states based on the resulting hydrogen-bonding patterns. For the primary analysis, these eight states were reduced to three: helix (H, G, I  $\rightarrow$  H, encompassing  $\alpha$ -helix,  $3_{10}$ -helix, and  $\pi$ -helix), sheet (E, B  $\rightarrow$  E, encompassing  $\beta$ -strand and  $\beta$ -bridge), and coil (T, S, blank  $\rightarrow$  C, encompassing turn, bend, and unstructured regions). This three-state reduction groups all helical subtypes together because the Hasimoto effective potential does not distinguish between them at the level of  $V_{re}[n]$ : all three helix types produce similar near-constant negative plateaus. For the structural correlate analysis in Sec. III, the original eight-state labels were also retained to distinguish  $\alpha$ -helix (H) from  $3_{10}$ -helix (G) and  $\pi$ -helix (I) at helix–coil boundaries. In the main dataset, the three-state distribution is 36.4% helix, 25.6% sheet, and 38.0% coil; within the helix class,  $\alpha$ -helix accounts for 31.8%,  $3_{10}$ -helix 4.1%, and  $\pi$ -helix 0.5% of all residues. Signal alignment between the Frenet-frame geometric quantities and DSSP labels used `dssp[2:N-2]`, trimming two residues from each end to match the index range of  $V_{re}[n]$  and  $E[n]$ .

TABLE I. Summary statistics of the two datasets. *Aligned residues* refers to positions for which  $V_{re}$ ,  $E$ , and DSSP labels are simultaneously available after Frenet-frame trimming.

	Main dataset	Helical peptides
Chains	1 986	251
Aligned residues	320 453	—
Length range	40–300	22–298
Mean length	165.4	106.5
Helix fraction	36.4%	83.4% (mean)
Sheet fraction	25.6%	—
Coil fraction	38.0%	—
Overlap with Ref. [27]	852 chains	—
Overlap with Ref. [28]	—	49 chains

For each chain, the discrete Frenet–Serret frame was computed from the  $C_\alpha$  trace following Refs. [27, 33]. Given  $N$   $C_\alpha$  coordinates  $\mathbf{r}[n]$  ( $n = 1, \dots, N$ ), the unit tangent vectors  $\mathbf{t}[n] = \Delta\mathbf{r}[n]/|\Delta\mathbf{r}[n]|$  were formed from successive differences  $\Delta\mathbf{r}[n] = \mathbf{r}[n+1] - \mathbf{r}[n]$ . The bond-angle curvature was computed as  $\kappa[n] = \arccos(\mathbf{t}[n] \cdot \mathbf{t}[n+1])$  ( $N-2$  values), and the dihedral torsion as  $\tau[n] = \text{atan2}((\hat{\mathbf{b}}[n] \times \hat{\mathbf{b}}[n+1]) \cdot \mathbf{t}[n+1], \hat{\mathbf{b}}[n] \cdot \hat{\mathbf{b}}[n+1])$  ( $N-3$  values), where  $\hat{\mathbf{b}}$  is the unit binormal vector obtained by normalizing  $\mathbf{t}[n] \times \mathbf{t}[n+1]$ . The DNLS effective potential components  $V_{re}[n]$  and  $V_{im}[n]$  were then computed from Eq. (1), and the integrability residual  $E[n]$  from Eq. (2), yielding  $L = N-4$  aligned values per chain (after trimming two residues from each end of the Frenet frame). The bond-length parameters  $\beta^\pm[n] = 1/b[n\pm 1]$  were computed from ac-

tual  $C_{\alpha}$ - $C_{\alpha}$  distances with no uniform-bond-length assumption (the standard  $C_{\alpha}$ - $C_{\alpha}$  distance is approximately 3.8 Å, but real structures exhibit small deviations due to peptide bond geometry and coordinate uncertainty), and the global average  $\beta = \frac{1}{2}(\langle \beta^+ \rangle + \langle \beta^- \rangle)$  was computed per chain. The curvature ratios  $r^{\pm}[n] = \kappa[n \pm 1]/\kappa[n]$  quantify the local uniformity of bending: in ideal helices  $r^{\pm} \approx 1$ , while in coil regions  $r^{\pm}$  can deviate substantially from unity. All formulas were verified to reproduce Ref. [27] results to machine precision ( $< 10^{-14}$ ) on the 852 overlapping chains. These spatial-domain geometric quantities provide the input signal for the frequency-domain analysis described next.

The short-time Fourier transform of  $V_{re}[n]$  was computed using `scipy.signal.stft` [34] with a Gaussian window of standard deviation  $\sigma$  (in residues). The Gaussian window was chosen because it achieves the minimum time-frequency uncertainty product  $\Delta t \cdot \Delta \omega = 1/2$ , providing the best simultaneous localization in both domains [29]. This is particularly important for protein backbone signals, where secondary structure segments can be as short as 3–4 residues ( $3_{10}$ -helices) and the transitions between them occur within 1–2 residues. The window length was set to  $M = \text{round}(6\sigma)$  (forced to the nearest odd integer), which captures 99.7% of the Gaussian weight, and the overlap was set to  $M-1$  (single-sample stride) to produce one spectral estimate per residue. No boundary padding was applied; consequently, the first and last  $\lfloor M/2 \rfloor$  residues of each chain lack STFT values and were excluded from all analyses. For the smallest window ( $\sigma = 1.5$ ,  $M = 9$ ), this trims 4 residues from each end, leaving  $\geq 96\%$  of residues in chains of length  $\geq 40$ . The local power spectral density at residue  $n$  is  $P(n, \omega_k; \sigma) = |S(n, \omega_k)|^2$ , where  $S$  denotes the STFT coefficient. The normalized spectral distribution is

$$\hat{P}(n, \omega_k; \sigma) = \frac{P(n, \omega_k; \sigma)}{\sum_{k'} P(n, \omega_{k'}; \sigma)}, \quad (3)$$

and the local spectral entropy is

$$H_{\text{spec}}[n; \sigma] = \frac{-\sum_k \hat{P}(n, \omega_k; \sigma) \ln \hat{P}(n, \omega_k; \sigma)}{\ln K}, \quad (4)$$

where  $K$  is the number of frequency bins, so that  $H_{\text{spec}} \in [0, 1]$ . Residues with zero total power were assigned  $H_{\text{spec}} = \text{NaN}$  and excluded from all analyses. The window width was swept over  $\sigma \in \{1.5, 2.0, 2.5, 3.0, 3.5, 4.0, 5.0, 6.0, 7.0, 8.0\}$  residues, spanning from the minimum that yields a meaningful spectrum ( $M = 9$  frequency bins at  $\sigma = 1.5$ ) to widths exceeding two full helical turns ( $\sigma = 8.0$ ,  $M = 48$ ). For each  $\sigma$ , the helix-vs-rest ROC AUC was computed across all aligned residues in the main dataset. The optimal  $\sigma^*$  was identified as the value maximizing AUC, and a cubic spline interpolation over the discrete  $\sigma$  grid was used to refine this estimate. To probe the complementary low-pass regime, we defined

$$R_{\text{LF}}[n; \sigma, f_c] = \frac{\sum_{|\omega_k| \leq f_c} P(n, \omega_k; \sigma)}{\sum_k P(n, \omega_k; \sigma)}, \quad (5)$$

measuring the fraction of local STFT power at or below a frequency cutoff  $f_c$ . When  $f_c = 0$ ,  $R_{\text{LF}}$  reduces to the DC

power fraction, which measures how much of the local signal energy is concentrated in the zero-frequency (mean-value) component. In helical segments, where  $V_{re}[n]$  is nearly constant, the DC component dominates and  $R_{\text{LF}}$  is large; in coil regions, where  $V_{re}[n]$  fluctuates rapidly, power is distributed across many frequency bins and  $R_{\text{LF}}$  is small. The optimal parameters were determined by grid search over  $\sigma \in \{1.5, 2.0, 2.5, \dots, 8.0\}$  and  $f_c$  ranging from 0 (DC only) to the Nyquist frequency in 20 equally spaced steps, maximizing the helix-vs-rest ROC AUC on the main dataset. To quantify complementarity between these indicators, we formed  $z$ -score standardized linear combinations  $S[n] = \alpha \tilde{X}_1 + (1-\alpha) \tilde{X}_2$ , where  $\tilde{X} = (X - \mu_X)/\sigma_X$  is the global  $z$ -score computed over all aligned residues in the main dataset. The  $z$ -score transformation ensures that both components contribute on a common scale regardless of their original units and dynamic ranges. The mixing weight  $\alpha^*$  was determined by sweeping  $\alpha \in [0, 1]$  in steps of 0.01 and selecting the value maximizing AUC. Two composite scores were constructed:  $S_{EH} = \alpha^* \tilde{E} + (1-\alpha^*) \tilde{H}_{\text{spec}}$  (combining the high-pass integrability residual with spectral entropy) and  $S_{ER} = \alpha^* \tilde{E} + (1-\alpha^*) \tilde{R}_{\text{LF}}$  (combining  $E[n]$  with the low-frequency energy ratio). Statistical significance of AUC improvements relative to  $E[n]$  alone was assessed by the DeLong test [35], which provides a non-parametric comparison of two correlated ROC curves by estimating the variance of the AUC difference through placement values.

Finally, helix-coil boundaries were identified as positions where the three-state DSSP label changes between H and non-H, yielding a total of 21 107 such boundaries across the 1986 chains; of these, 2351 were discarded because they fell within 10 residues of a chain terminus, leaving 18 756 boundaries with complete  $\pm 10$ -residue windows (an additional 392 boundaries with partial windows were successfully fitted, yielding 19 148 valid boundaries in total for the spectral entropy analysis). For each boundary, a sigmoid function  $f(n) = L/(1 + e^{-k(n-n_0)}) + b$  was fitted to the  $H_{\text{spec}}[n]$  profile in a  $\pm 10$ -residue window centered on the boundary, using nonlinear least squares (`scipy.optimize.curve_fit`). The four parameters are:  $L$  (excursion amplitude),  $k$  (steepness),  $n_0$  (midpoint position), and  $b$  (baseline offset). The transition width was defined as the 20%–80% excursion width  $w = 2 \ln 4/|k|$ , which measures the number of residues over which the spectral entropy completes the bulk of its jump:  $w \ll 1$  indicates a discontinuous (first-order-like) transition, while  $w \gg 1$  indicates a gradual crossover. The excursion amplitude  $|L|$  measures the magnitude of the spectral entropy change across the boundary. Boundaries were classified as helix-entry (C→H) or helix-exit (H→C) to test for directional asymmetry, and the Mann-Whitney  $U$  test [36] with rank-biserial correlation as effect size was used to compare transition width distributions between the two directions.

### III. RESULTS

Figure 2 illustrates the STFT analysis for a representative protein chain. The  $V_{re}[n]$  trace exhibits the character-

istic pattern identified in Ref. [27]: near-constant negative plateaus in  $\alpha$ -helical segments and large-amplitude broadband fluctuations in coil regions. The STFT spectrogram  $|S(n, \omega; \sigma=1.5)|^2$  makes this contrast visually explicit: helical segments appear as narrow vertical bands concentrated at the DC frequency, while coil regions fill the full frequency axis. The spectral entropy  $H_{\text{spec}}[n]$  tracks this distinction as a single scalar: low values ( $H_{\text{spec}} \lesssim 0.3$ ) within helices, rising sharply to  $H_{\text{spec}} \gtrsim 0.5$  at helix-coil boundaries.

Across the full dataset of 320 453 residues, the mean spectral entropy at  $\sigma = 1.5$  consistently orders as  $\langle H_{\text{spec}} \rangle_{\text{helix}} = 0.440 < \langle H_{\text{spec}} \rangle_{\text{sheet}} = 0.483 < \langle H_{\text{spec}} \rangle_{\text{coil}} = 0.513$  (Fig. 3a). The helix-coil separation has Cohen’s  $d \approx 0.65$  [37], indicating a medium-to-large effect size. This three-level ordering reflects the underlying spectral structure of  $V_{\text{re}}[n]$  in each secondary structure class. In helical segments, the near-constant  $V_{\text{re}}$  (mean  $\mu_H = -0.250 \text{ \AA}^{-2}$ , variance  $\sigma_H^2 = 0.021$ ) concentrates the majority of STFT power at the DC frequency, producing a sharply peaked power spectrum and low entropy. In coil regions, the large-amplitude fluctuations ( $\mu_C = -0.611$ ,  $\sigma_C^2 = 0.084$ ) distribute power across the full frequency axis, yielding a flatter spectrum and higher entropy. Sheet residues ( $\mu_E = -0.873$ ,  $\sigma_E^2 = 0.070$ ) occupy an intermediate position: their  $V_{\text{re}}$  values are more negative on average than coil but exhibit less broadband variability than coil, placing their spectral entropy between the two extremes.

The ordering is robust: it holds across all 1986 individual chains and persists across all stratification layers (by helix content, chain length, and dataset origin; Table II). As a binary helix-vs-rest classifier,  $H_{\text{spec}}$  at  $\sigma^* = 1.5$  achieves ROC AUC = 0.715, compared with AUC = 0.783 for  $E[n]$  (Fig. 3b). The AUC gap of  $-0.068$  is consistent across all strata ( $\Delta\text{AUC}$  ranges from  $-0.035$  to  $-0.073$ ; Table II), confirming that  $E[n]$  is the most effective single-residue detector among those tested. The high-helix stratum achieves the highest absolute AUC for both indicators ( $\text{AUC}_E = 0.823$ ,  $\text{AUC}_H = 0.774$ ), while the low-helix stratum yields the smallest gap ( $\Delta\text{AUC} = -0.035$ ), suggesting that the relative advantage of  $E[n]$  is most pronounced when helical segments are abundant and well-separated.

TABLE II. Stratified ROC AUC for  $E[n]$  and  $H_{\text{spec}}[n; \sigma=1.5]$  across dataset subgroups.  $\Delta\text{AUC} = \text{AUC}_H - \text{AUC}_E$  is negative in all strata.

Stratum	Group	AUC( $E$ )	AUC( $H_{\text{spec}}$ )	$\Delta\text{AUC}$
Overall	All	0.783	0.715	$-0.068$
Helix %	Low	0.664	0.629	$-0.035$
	Mid	0.772	0.706	$-0.066$
	High	0.823	0.774	$-0.049$
Length	Short	0.813	0.756	$-0.057$
	Medium	0.782	0.717	$-0.065$
	Long	0.779	0.706	$-0.073$
Origin	Ref. [27]	0.782	0.711	$-0.071$
	New	0.784	0.718	$-0.066$

Given that  $H_{\text{spec}}$  discriminates secondary structure types at  $\sigma = 1.5$ , we next investigated whether a larger window width improves performance by better resolving the periodic struc-

ture of helices. Figure 4a shows the ROC AUC and Youden’s  $J$  statistic as functions of the STFT window width  $\sigma$ . The AUC decreases monotonically from 0.715 at  $\sigma = 1.5$  to 0.441 at  $\sigma = 8.0$ , with no local maximum at any intermediate scale. Youden’s  $J$  peaks at  $\sigma = 2.0$  ( $J = 0.392$ ), marginally above  $\sigma = 1.5$  ( $J = 0.381$ ), but both values correspond to sub-turn scales ( $\sigma = 1.5$  residues  $\approx 0.42$  helical turns). At  $\sigma \geq 3.0$ , the Gaussian window extends beyond the ends of short chains, producing undefined values for edge residues: the NaN fraction grows from 10.5% at  $\sigma = 3.0$  to 29.0% at  $\sigma = 8.0$ , further degrading the practical utility of wide windows. The absence of a peak near one helical period ( $\sigma \approx 3.6$ ) indicates that the helix-coil discrimination does not rely on resolving the periodic structure of helices; rather, it depends on detecting the local spectral contrast between ordered and disordered geometry.

This monotonic decay can be understood through a piecewise-stationary signal model. We model  $V_{\text{re}}[n]$  as alternating segments of constant mean  $\mu_H$  (helix) and  $\mu_C$  (coil) with additive noise. The intrinsic discriminability between the two classes, measured by the squared standardized mean difference  $d_{\text{int}}^2(\sigma)$ , increases with  $\sigma$  because wider windows average out noise. However, the fraction of residues whose STFT window straddles a helix-coil boundary also grows: at  $\sigma = 1.5$ , approximately 53% of residues are boundary-contaminated (within  $3\sigma$  of a transition), rising to 88% at  $\sigma = 8.0$ . The effective discriminant  $d_{\text{eff}}^2 \propto (1 - f_{\text{bnd}})^2 d_{\text{int}}^2$  is dominated by the contamination fraction and decreases monotonically, reproducing the observed AUC trend (Spearman  $\rho = 0.81$ ,  $p = 0.004$ ; Fig. 4b).

Stratified validation by boundary distance  $d_{\text{bnd}}$  confirms this picture. For boundary residues ( $d_{\text{bnd}} = 0$ ), AUC is near chance (0.52–0.58) at all  $\sigma$ . For interior residues ( $d_{\text{bnd}} = 5$ –7), AUC peaks at  $\sigma = 3.5$  (AUC = 0.912), while for deeply buried residues ( $d_{\text{bnd}} \geq 8$ ) the peak shifts to  $\sigma = 5.0$  (AUC = 0.901). The rightward shift of the optimal  $\sigma$  with increasing  $d_{\text{bnd}}$  reflects the balance between frequency-resolution gain and boundary contamination: deeper interior residues tolerate wider windows before the nearest boundary enters the  $3\sigma$  support. This establishes a maximal-localization constraint: the overall AUC is maximized at the smallest  $\sigma$  because the majority of residues in real proteins lie close to a helix-coil boundary.

The maximal-localization constraint explains why AUC decreases with  $\sigma$ , but it does not explain why the spectral entropy ordering helix  $<$  sheet  $<$  coil holds in the first place. A naive piecewise-stationary model with white noise predicts an inverted spectral entropy ordering ( $H_{\text{spec}}^{\text{helix}} > H_{\text{spec}}^{\text{coil}}$ ). This discrepancy arises because non-helical segments have a larger mean  $|\mu_C|$  in  $V_{\text{re}}[n]$  than helical segments ( $|\mu_{\text{nonH}}| = 0.716$  vs.  $|\mu_H| = 0.250 \text{ \AA}^{-2}$ ). In a white-noise model, this larger DC offset concentrates more power at the zero-frequency bin, which lowers the spectral entropy (making the distribution more peaked) relative to helical segments. Under this model, coil regions would paradoxically appear more spectrally ordered than helices. At  $\sigma = 1.5$ , the white-noise model predicts  $H_{\text{spec}}^{\text{helix}} = 0.598$  and  $H_{\text{spec}}^{\text{nonH}} = 0.528$ , inverting the empirically observed ranking.

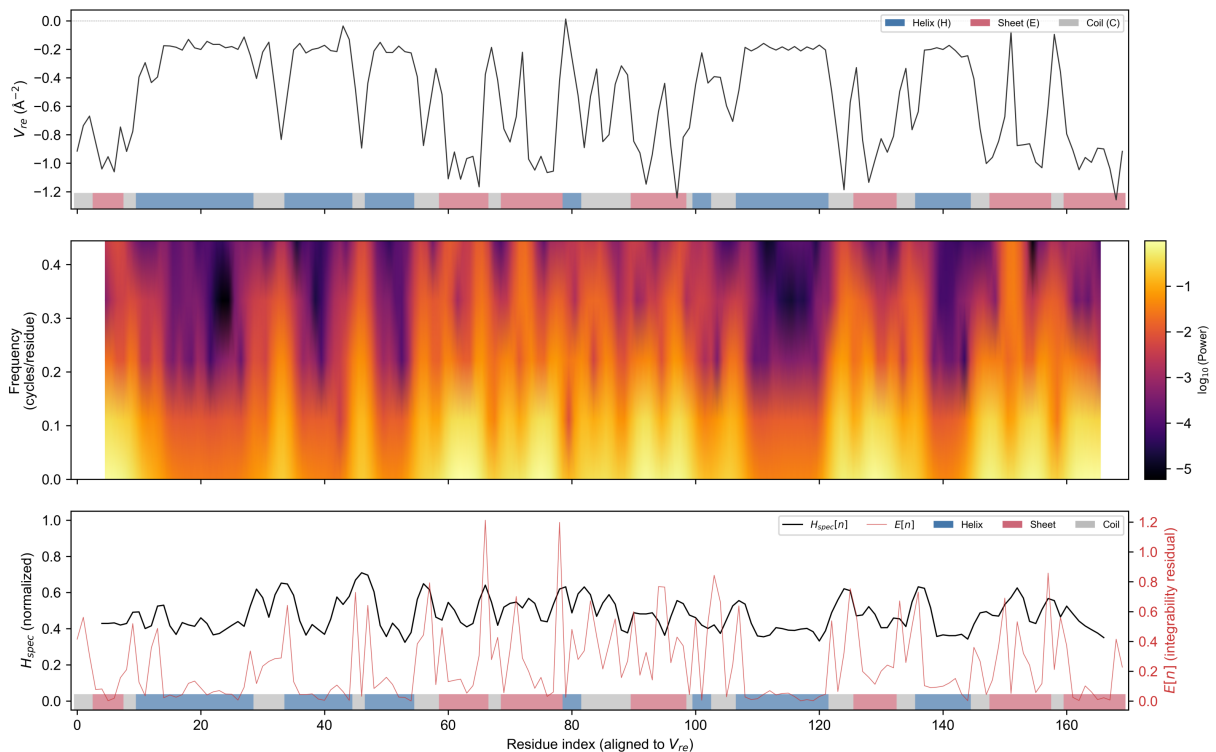


FIG. 2. Short-time Fourier transform (STFT) analysis of the Hasimoto potential  $V_{re}[n]$  for protein chain 8OSP\_A ( $N = 174$  residues,  $\sigma = 1.5$ ). Top:  $V_{re}[n]$  trace along the backbone ( $L = 170$  after end trimming), with DSSP secondary structure annotation shown as a color ribbon (blue = helix, red = sheet, gray = coil). Middle: STFT power spectrogram  $|\mathcal{S}(n, \omega)|^2$  computed with a Gaussian window (nperseg = 9, 5 frequency bins, 162 time frames), displayed on a  $\log_{10}$  scale. Helical regions exhibit concentrated low-frequency power, while coil regions show broadband energy dispersion. Bottom: Normalized spectral entropy  $H_{\text{spec}}[n] \in [0, 1]$  (black, left axis) and integrability residual  $E[n]$  (red, right axis), with 163 of 170 residue positions covered by the STFT window. The mean  $H_{\text{spec}}$  follows the ordering helix (0.444) < sheet (0.484) < coil (0.523), consistent with the expectation that structurally ordered regions produce lower spectral entropy. Note the smoother profile of  $H_{\text{spec}}$  due to the STFT window averaging, contrasting with the pointwise sensitivity of  $E[n]$ ; this high-pass/low-pass complementarity motivates the composite score analysis in Sec. III.

This apparent contradiction is resolved by incorporating the empirical short-range autocorrelation of  $V_{re}[n]$ . We fitted an AR(1) colored-noise model with lag-1 autocorrelation  $\rho \approx 0.25$  separately to helical and non-helical residues. However, even the AR(1) model fails to reproduce the correct ordering: at  $\sigma = 1.5$ , it predicts  $H_{\text{spec}}^{\text{helix}} = 0.552 > H_{\text{spec}}^{\text{nonH}} = 0.494$ , still inverted. Only the full empirical spectral shape model, which preserves the measured frequency-dependent power distribution of each class, yields the correct ranking ( $H_{\text{spec}}^{\text{helix}} = 0.686 > H_{\text{spec}}^{\text{nonH}} = 0.608$  in absolute terms, but with the analytical null model giving  $H_{\text{spec}}^{\text{helix}} = 0.496 < H_{\text{spec}}^{\text{nonH}} = 0.564$ ). The physical origin is that non-helical  $V_{re}$  fluctuations are genuinely broadband (colored noise with significant power across all frequencies), not merely large-amplitude white noise. The empirical spectral flatness of non-helical residues (0.69–0.78, depending on  $\sigma$ ) substantially exceeds that of helical residues (0.44–0.51), confirming that coil regions distribute power more uniformly across frequencies. It is this spectral bandwidth difference, rather than the DC level alone, that drives the entropy separation between secondary structure types. This result underscores that the spectral entropy ordering is a non-trivial property of the backbone geometry, not a simple consequence

of signal amplitude differences.

With the physical origin of the entropy ordering identified, we quantify the relationship between the two geometric indicators. The residue-level Spearman rank correlation between  $H_{\text{spec}}[n; \sigma=1.5]$  and  $E[n]$  across all 320 453 residues is  $\rho = 0.454$  ( $p < 10^{-308}$ , the IEEE 754 float64 underflow limit; Fig. 6a). This moderate value indicates that the two indicators capture related but non-redundant geometric information. The relationship is expected because both quantities respond to the spectral structure of  $V_{re}[n]$ :  $E[n]$  is a pointwise high-pass filter sensitive exclusively to nearest-neighbor torsion differences, whereas  $H_{\text{spec}}$  integrates spectral content over a  $6\sigma \approx 9$ -residue window and summarizes the full bandwidth of the local power spectrum. The moderate correlation ( $\rho = 0.454$ ) indicates that  $H_{\text{spec}}$  captures spectral information not accessible to the pointwise operator  $E[n]$ , motivating the composite score analysis below.

Per-chain analysis on the 251 helical peptides yields a mean Spearman  $\rho = 0.424$  (median 0.487), with 94.8% of chains showing  $\rho > 0$ , confirming that the positive association is consistent across individual proteins. The nature of the non-redundant information is clarified by a segment-level analy-

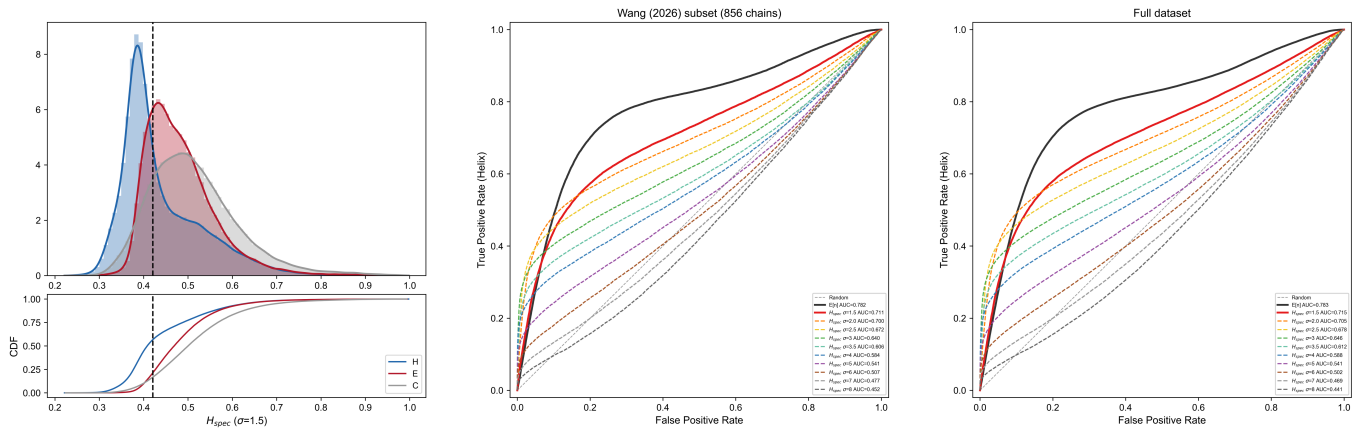


FIG. 3. Statistical characterization of spectral entropy  $H_{\text{spec}}$  for helix detection across 2 060 non-redundant protein chains (320 453 residues). (a) Left top: Probability density (histogram + KDE) of  $H_{\text{spec}}$  at  $\sigma = 1.5$  for helix (H, blue;  $n = 116\,646$ ), sheet (E, red;  $n = 82\,043$ ), and coil (C, gray;  $n = 121\,764$ ) residues. The dashed line marks the Youden-optimal threshold  $\theta^* = 0.421$  [38]. Cohen’s  $d$  (H vs. non-H) = 0.652. Left bottom: Empirical CDF of  $H_{\text{spec}}$  by secondary structure class, confirming the stochastic ordering  $H \prec E \prec C$ . (b, c) ROC curves for helix-vs-non-helix classification on the Wang (2026) 856-chain subset and the full dataset, respectively. In both panels, the black curve shows the  $-E[n]$  baseline (AUC  $\approx 0.783$ ), and colored curves show  $-H_{\text{spec}}$  at  $\sigma \in \{1.5, 2.0, 2.5, 3.0, 3.5, 4.0, 5.0, 6.0, 7.0, 8.0\}$ . The best spectral-entropy classifier ( $\sigma^* = 1.5$ , AUC = 0.715) is shown as a solid line; all others are dashed. The spectral-entropy classifier underperforms  $E[n]$  in pointwise helix detection, consistent with the low-pass nature of the STFT smoothing; however, this gap is closed by the composite score (Sec. III). The monotonic decrease of AUC with increasing  $\sigma$  is consistent with the maximal-localization constraint (Sec. III).

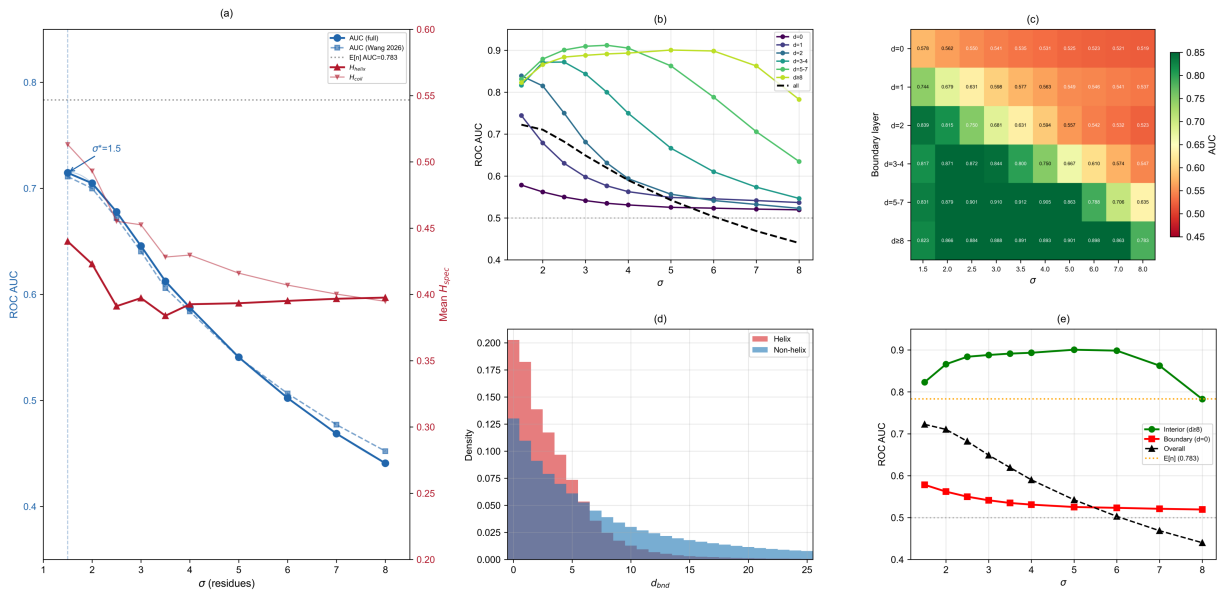


FIG. 4. (a) ROC AUC (blue) and Youden’s  $J$  (orange) as functions of STFT window width  $\sigma$ . Both metrics indicate optimal performance at the smallest tested  $\sigma$ , with monotonic decay thereafter. (b) Piecewise-stationary model prediction of  $d_{\text{eff}}^2(\sigma)$  (dashed) versus empirical AUC (solid), showing that boundary contamination accounts for the monotonic decay (Spearman  $\rho = 0.81$ ).

sis using the Jensen–Shannon divergence (JSD) [39] between each helical segment’s STFT power spectrum and the ideal DNLS soliton spectrum. The JSD correlates strongly with  $H_{\text{spec}}$  ( $\rho = 0.800$ ) but only moderately with  $E[n]$  ( $\rho = 0.522$ ), and partial correlation analysis confirms that JSD carries independent frequency-domain information beyond  $E[n]$ : the partial correlation JSD vs.  $H_{\text{spec}}$  controlling for  $E[n]$  is  $+0.766$ , whereas JSD vs.  $E[n]$  controlling for  $H_{\text{spec}}$  drops to  $+0.407$ .

The JSD serves as a close proxy for spectral flatness ( $\rho = 0.948$ ), indicating that the non-redundant content of  $H_{\text{spec}}$  relative to  $E[n]$  is predominantly the broadband character of the local power spectrum rather than any single-frequency feature.

The moderate correlation between these two indicators reflects their distinct spatial resolutions, motivating a quantitative characterization of the helix–coil boundary sharpness.

Sigmoid fits to 21,107 helix–coil boundaries across the 1,986 chains reveal that the spectral entropy transition is remarkably sharp (Fig. 5a). The median transition width is  $w = 0.145$  residues, and 85.3% of boundaries have  $w \leq 1$  residue (Fig. 5b). A further 8.5% fall in the range  $1 < w \leq 3$  residues, and only 6.2% exceed 3 residues. This sub-residue sharpness is characteristic of an abrupt, step-like transition rather than a gradual crossover. The median sigmoid steepness parameter is  $k = 19.1$ , corresponding to a transition that is effectively complete within a single residue step.

A significant directional asymmetry exists: helix-exit (H→C) boundaries are sharper than helix-entry (C→H) boundaries, with median transition widths of 0.142 and 0.149 residues respectively (Mann–Whitney  $p = 1.4 \times 10^{-25}$ , rank-biserial  $r = 0.087$ ). Although the effect size is small in absolute terms, the extreme statistical significance (reflecting  $N = 19,148$  valid boundaries) establishes the asymmetry as a genuine structural feature. This asymmetry is consistent with the known difference in helix capping mechanisms [40]: C-terminal helix termination involves the concerted loss of several  $i \rightarrow i+4$  hydrogen bonds, whereas N-terminal nucleation requires their sequential establishment, producing a slightly more gradual geometric onset.

The 6.2% of boundaries with  $w > 3$  residues (the distribution tail) do not correspond to longer helices or higher integrability residuals: their median helix length and mean  $E[n]$  are indistinguishable from the sharp majority. However, their spectral entropy excursion  $|L|$  is approximately 2.0 times larger than that of sharp boundaries (0.117 vs. 0.058), indicating that these gradual transitions involve a larger absolute change in local spectral character spread over more residues. Among tail boundaries, C→H entries are overrepresented (59%), consistent with the directional asymmetry noted above.

The sharpness is effectively invariant to helix type ( $\alpha$ ,  $3_{10}$ ,  $\pi$ ), adjacent secondary structure element, and helix length: although Kruskal–Wallis tests [41] reach nominal significance for helix type ( $p = 0.032$ ) and helix length ( $p = 10^{-7}$ ), the effect sizes are negligible (rank-biserial  $|r| < 0.02$ ; Spearman  $\rho = 0.042$ ), suggesting that sharpness is largely an intrinsic geometric property of the helix–coil interface rather than a context-dependent feature.

The sub-residue sharpness of these boundaries, combined with the moderate  $H_{\text{spec}}-E[n]$  correlation ( $\rho = 0.454$ ), suggests that combining the two indicators may improve helix detection beyond what either achieves alone. To quantify this complementarity, we formed a  $z$ -score linear combination  $S = \alpha \tilde{E} + (1-\alpha)\tilde{H}$ , where  $\tilde{E}$  and  $\tilde{H}$  denote globally standardized (zero mean, unit variance) versions of  $-E[n]$  and  $-H_{\text{spec}}[n]$  respectively (negated so that higher values indicate helix). The mixing weight was optimized over  $\alpha \in [0, 1]$  in steps of 0.01, yielding  $\alpha^* = 0.84$  and  $\text{AUC} = 0.803$  ( $\Delta\text{AUC} = +0.020$  over  $E[n]$  alone; DeLong  $p < 10^{-100}$ ; Fig. 6b). The high optimal weight on  $E[n]$  ( $\alpha^* = 0.84$ ) reflects its superior discriminative power, but the statistically significant improvement confirms that  $H_{\text{spec}}$  contributes non-redundant information. The improvement is consistent across all six stratification layers ( $\Delta\text{AUC}$  ranges from +0.015 to +0.026; Table III).

TABLE III. Composite score stratified validation.  $S_{EH} = 0.84\tilde{E} + 0.16\tilde{H}$  and  $S_{ER} = 0.81\tilde{E} + 0.19\tilde{R}_{\text{LF}}$ .  $\Delta\text{AUC}$  is relative to  $E[n]$  alone in each stratum. Strata are defined by terciles of chain length and helix fraction.

Stratum	AUC( $E$ )	AUC( $S_{EH}$ ) / $\Delta$	AUC( $S_{ER}$ ) / $\Delta$
Overall	0.783	0.803 / +0.020	0.815 / +0.032
Helix% Low	0.696	0.711 / +0.015	0.728 / +0.032
Helix% High	0.810	0.836 / +0.026	0.846 / +0.036
Short chains	0.797	0.820 / +0.023	0.828 / +0.031
Long chains	0.779	0.798 / +0.019	0.811 / +0.032
Ref. [27] subset	0.782	0.801 / +0.019	0.814 / +0.032

The connection to soliton physics deepens the interpretation of this complementarity. The Jensen–Shannon divergence (JSD) between each helical segment’s STFT power spectrum and the ideal soliton (pure DC) reference correlates very strongly with the Wiener spectral flatness [42] ( $\rho = 0.948$ ). Partial correlation analysis confirms that JSD carries substantial frequency-domain information beyond  $E[n]$ : the partial correlation JSD vs.  $H_{\text{spec}}$  controlling for  $E[n]$  is +0.766, whereas controlling for JSD reduces the  $E[n]-H_{\text{spec}}$  correlation to  $-0.095$ .

To probe the complementary low-pass regime, we computed the low-frequency energy ratio  $R_{\text{LF}}[n; \sigma, f_c]$  (Eq. 5), which measures the fraction of local STFT power concentrated at or below a frequency cutoff  $f_c$ . A grid search over  $\sigma \in \{1.5, 2.0, \dots, 8.0\}$  and all available frequency bins reveals that the optimal parameters are  $\sigma = 2.0$  and  $f_c = 0$  (DC bin only), yielding a standalone  $\text{AUC} = 0.727$ . This is below  $E[n]$  (0.783) but above  $H_{\text{spec}}$  (0.715), indicating that the DC fraction alone carries substantial discriminative information. The  $E-R_{\text{LF}}$  composite  $S_{\text{LF}} = 0.81\tilde{E} + 0.19\tilde{R}_{\text{LF}}$  achieves  $\text{AUC} = 0.815$  ( $\Delta\text{AUC} = +0.032$ ; DeLong  $p < 10^{-100}$ ; Fig. 7), surpassing the  $E-H_{\text{spec}}$  composite. The optimality of  $f_c = 0$  confirms that the discriminative information in the low-frequency regime is concentrated predominantly at zero frequency: helical segments have a larger DC fraction because their  $V_{\text{re}}[n]$  is dominated by the constant negative plateau. The high-pass  $E[n]$  and low-pass  $R_{\text{LF}}$  thus form a dual pair of frequency-domain probes.

The preceding analyses establish that the pointwise high-pass filter  $E[n]$  and the windowed spectral entropy  $H_{\text{spec}}$  capture substantially complementary frequency-domain information. To demonstrate the macroscopic 3D consequences of this 1D signal duality, we apply the analytic reconstruction framework from Ref. [28]. Here, we use 3D root-mean-square deviation (RMSD) not as a predictive benchmark, but as a macroscopic readout to physically manifest the Gabor time-frequency uncertainty principle.

Applying the  $E[n] > 0.10$  high-pass threshold yields a global topological reconstruction success rate of 72.9% ( $\text{RMSD} < 2 \text{ \AA}$ ) on the 251 helical peptide dataset. In contrast, the optimally thresholded spectral indicator ( $H_{\text{spec}} > \theta^*$ ) achieves only 57.4%. This 15.5 percentage-point gap illustrates the macroscopic 3D consequence of the spatial-spectral constraint (Sec. III): the STFT window inevitably blurs the

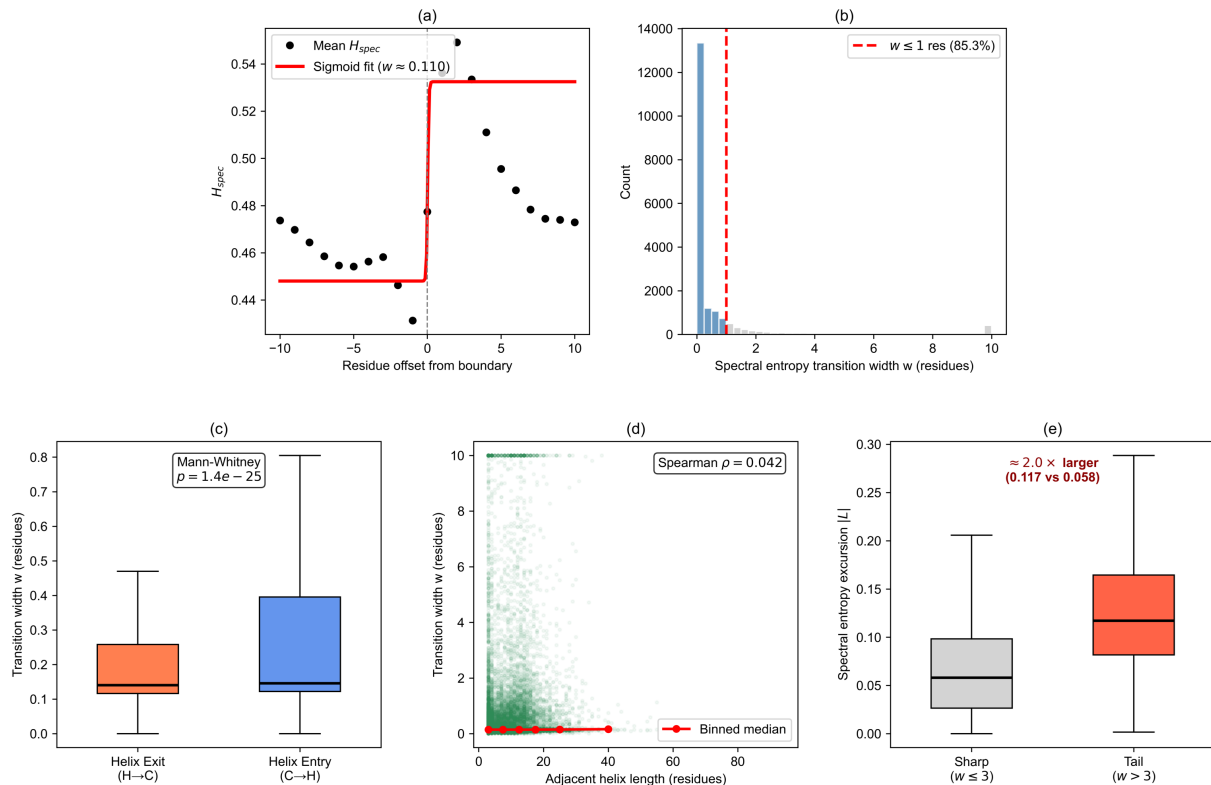


FIG. 5. Abrupt geometric transition at helix-coil boundaries. (a) Representative sigmoid fit (red curve) to the local spectral entropy  $H_{\text{spec}}$  profile (black dots) at a single helix-coil boundary. (b) Distribution of the fitted transition widths  $w$  across 21 107 boundaries. The vertical dashed line marks  $w = 1$  residue; 85.3% of boundaries fall below this sub-residue limit. (c) Directional asymmetry in transition sharpness. Helix-exit (H→C) boundaries are statistically sharper than helix-entry (C→H) transitions (Mann-Whitney  $p = 1.4 \times 10^{-25}$ ). (d) Transition width  $w$  shows no meaningful correlation with the adjacent helix length (Spearman  $\rho = 0.042$ ). (e) Physical characterization of the distribution tail ( $w > 3$  residues). These gradual boundaries exhibit a spectral entropy excursion  $|L|$  approximately 2.0 times larger (median  $\approx 0.117$ ) than that of the sharp majority (median  $\approx 0.058$ ), indicating that the broader spatial transition is driven by a larger absolute jump in local spectral disorder.

remarkably sharp, sub-residue abrupt boundaries that  $E[n]$  resolves with high fidelity, leading to terminal fraying and degraded RMSD in globally clean helices.

However, case studies reveal a notable vulnerability of the high-pass limit that spectral filtering can mitigate. On sequences contaminated with high-frequency geometric noise, such as isolated torsion sign-flips or local structural bends, the sensitivity of  $E[n]$  triggers substantial over-segmentation. For instance, in the coiled-coil ITQG\_A (Fig. 8c), local torsion fluctuations cause  $E[n]$  to fragment a continuous macroscopic helix into five disconnected segments, increasing the 3D RMSD to 15.27 Å. Conversely, the STFT window of  $H_{\text{spec}}$  functions as a low-pass smoother that suppresses these high-frequency local defects, preserving the underlying continuous DC-band structure and recovering the global helical topology (RMSD = 0.87 Å). A similar recovery is observed in the villin headpiece (2F4K\_A, Fig. 8b), where  $H_{\text{spec}}$  improves the RMSD by 3.91 Å by smoothing over localized noise.

These 3D reconstructions illustrate that no single spatial filter is globally optimal under the spatial-spectral uncertainty principle. Absolute boundary precision (requiring a pointwise high-pass filter) and global topological noise immunity (re-

quiring a wide-band smoothing window) cannot be achieved simultaneously. We attempted an adaptive routing strategy, using per-chain torsion standard deviation  $\sigma_\tau$  to explicitly choose between  $E[n]$  and  $H_{\text{spec}}$  for each chain. This failed to improve the global success rate beyond 72.9%, despite an oracle upper bound of 84.1%, motivating the simultaneous dual-probe approach (Fig. 1) rather than a binary per-chain algorithmic choice.

#### IV. DISCUSSION & CONCLUSIONS

The spectral dichotomy between DC-dominated helical segments and broadband coil regions, established quantitatively in Sec. III, provides a frequency-domain rationale for the empirical success of the pointwise integrability residual  $E[n]$  [27, 28]: as a high-pass operator,  $E[n]$  suppresses the helical DC plateau and amplifies boundary discontinuities. Combined with the sub-residue sharpness of helix-coil transitions, this dichotomy renders any finite-width spectral window susceptible to boundary contamination, establishing the signal-processing trade-off between boundary precision and

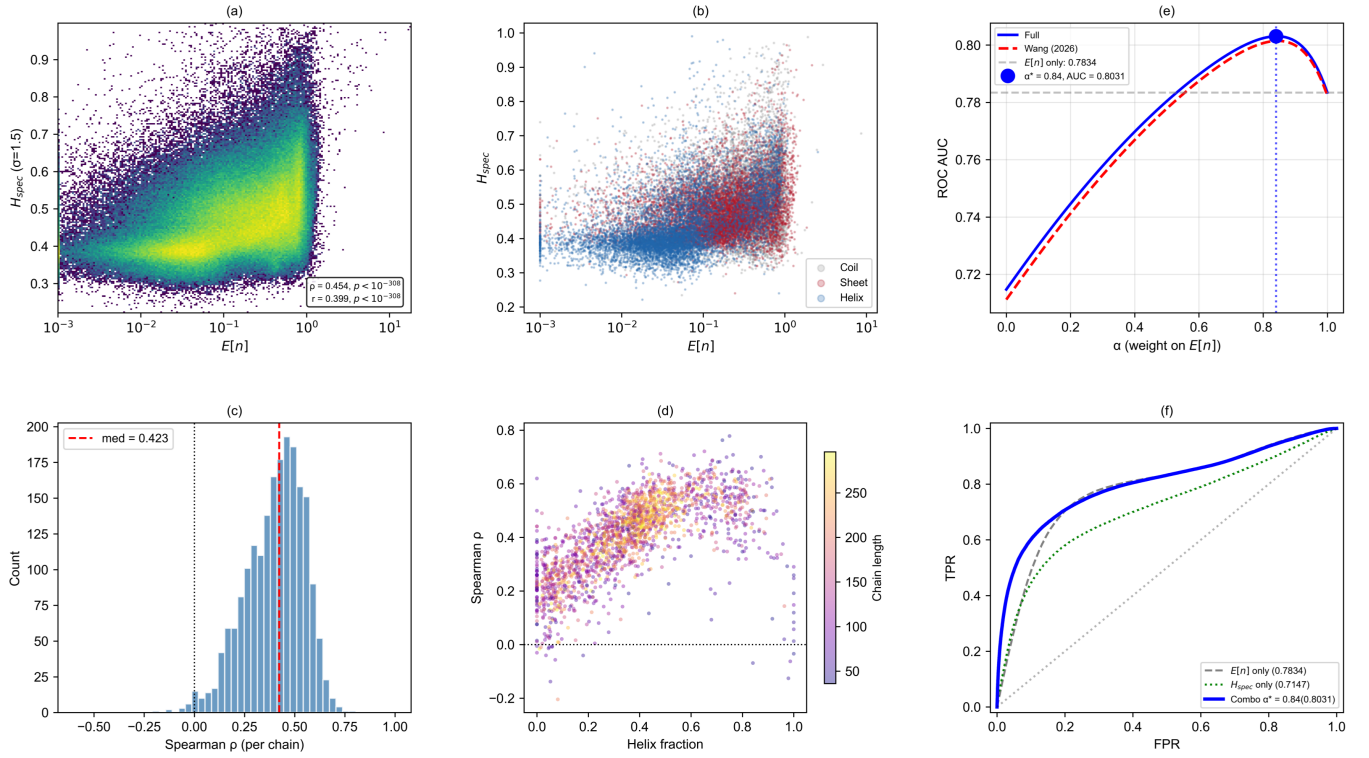


FIG. 6. Correlation between spectral entropy  $H_{\text{spec}}$  and integrability residual  $E[n]$ , and their combined helix-prediction performance. (a) Density scatter plot of  $H_{\text{spec}}$  ( $\sigma^* = 1.5$ ) versus  $E[n]$  for all 320,453 valid residues (log-scaled x-axis). Global Spearman  $\rho = 0.454$  and Pearson  $r = 0.399$  (both  $p < 10^{-308}$ ). (b) Same scatter colored by DSSP secondary-structure assignment: helix (H, blue), sheet (E, red), and coil (C, gray); per-class Spearman  $\rho = 0.472$  (H), 0.261 (E), 0.147 (C). (c) Histogram of per-chain Spearman  $\rho$  across 1,986 chains (median = 0.423; 99.1% of chains show  $\rho > 0$ ; 76.2% show  $\rho > 0.3$ ). (d) Per-chain Spearman  $\rho$  versus helix fraction, colored by chain length; positive correlation is strongest for helix-rich chains. (e) ROC AUC for helix-vs-non-helix classification as a function of the mixing weight  $\alpha$  in the combo score  $S^* = \alpha E + (1 - \alpha) H$ . The optimum  $\alpha^* = 0.84$  yields AUC = 0.803 on the full dataset (blue solid) and  $\alpha^* = 0.85$ , AUC = 0.802 on the Wang (2026) 856-chain subset (red dashed), compared with AUC = 0.783 for  $E[n]$  alone (gray dashed). (f) ROC curves at the optimal mixing weight: the combo score (blue solid, AUC = 0.803) outperforms both  $E[n]$  only (gray dashed, AUC = 0.783) and  $H_{\text{spec}}$  only (green dotted, AUC = 0.715).

topological noise immunity.

This intrinsic trade-off dictates that relying solely on the pointwise high-pass limit is topologically fragile: isolated torsion defects within an otherwise continuous helix trigger over-segmentation of the macroscopic topology. Conversely, widening the observation window to absorb such local noise inevitably blurs the sub-residue boundaries. In the language of integrable systems, an ideal discrete nonlinear Schrödinger (DNLS) soliton propagates without dispersing its spectral content, producing minimal spectral entropy; real helices approximate this limit. The high-pass channel ( $E[n]$ ) detects the rupture of this near-integrability at boundaries and defects, while the low-pass channel ( $R_{\text{LF}}$ ) measures the preservation of the DC-dominated spectral core within helical interiors. Their combination captures complementary frequency-domain information not fully accessible to either probe alone, improving the detection area under the curve from 0.783 to 0.815.

The sub-residue sharpness of helix-coil transitions (median width  $w = 0.145$  residues across 19,148 fitted boundaries) requires careful physical interpretation. On the discrete peptide lattice, this value means that the sigmoid transition in spec-

tral entropy is effectively complete between one  $C_\alpha$  position and the next, with no intermediate so-called half-helical state; the fitted continuous width should therefore be understood as a measure of the abruptness of the underlying discrete jump rather than as a literal sub-atomic spatial extent. This step-like character finds a natural thermodynamic counterpart in the Zimm-Bragg helix-coil model [43], where the small nucleation parameter ( $\sigma_{\text{ZB}} \ll 1$ ) compresses the coexistence region to one or two residues. The sub-residue geometric sharpness observed here provides an independent, purely kinematic observation consistent with this high degree of thermodynamic cooperativity and with the backbone conformational entropy change  $\Delta S_{\text{BB}} = 5.2 \pm 0.3 \text{ cal mol}^{-1} \text{ K}^{-1}$  per residue recently measured by calorimetry for the helix-to-coil transition [44]. The directional asymmetry quantified in Sec. III (helix exits being sharper than helix entries) is likewise consistent with the cooperative thermodynamics of the Zimm-Bragg framework, in which the free-energy landscape for helix propagation differs from that for nucleation [45], providing a macroscopic energetic context for the local hydrogen-bond kinematic mechanism identified therein.

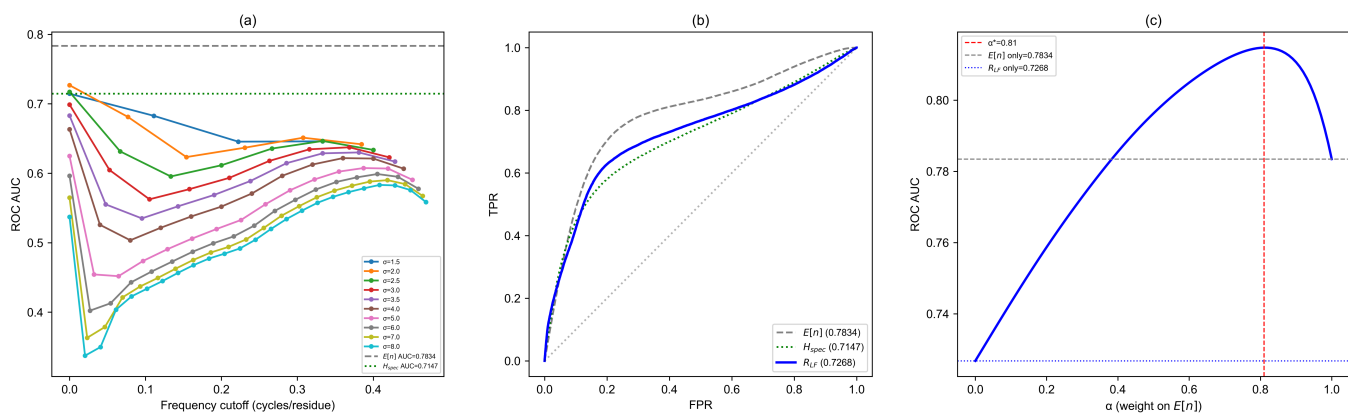


FIG. 7. Low-frequency energy ratio  $R_{LF}$  as a helix detector. (a) ROC AUC of  $R_{LF}$  as a function of frequency cutoff  $f_c$  for ten Gaussian window widths ( $\sigma = 1.5$ – $8.0$ ). Dashed gray and dotted green lines mark the baseline AUCs of  $E[n]$  (0.7834) and  $H_{\text{spec}}$  (0.7147), respectively. For all  $\sigma$ , the best AUC is achieved at  $f_c = 0$  (DC-only bin), with  $\sigma = 2.0$  yielding the highest single-cutoff AUC of 0.7268. Larger  $\sigma$  values progressively degrade discrimination, consistent with over-smoothing of the local spectral structure. (b) ROC curves for the best  $R_{LF}$  configuration ( $\sigma = 2.0$ ,  $f_c = 0.000$ ) compared with  $E[n]$  and  $H_{\text{spec}}$  baselines.  $R_{LF}$  alone (AUC = 0.7268) falls below  $E[n]$  (0.7834) but slightly exceeds  $H_{\text{spec}}$  (0.7147). (c) AUC of the linear combination  $S = \alpha \cdot E[n]_z + (1 - \alpha) \cdot R_{LF,z}$  as a function of the mixing weight  $\alpha$ . The optimum at  $\alpha^* = 0.81$  achieves AUC = 0.8147, a gain of +0.0313 over  $E[n]$  alone, indicating that  $R_{LF}$  captures complementary spectral information not fully encoded in the per-residue energy.

This geometric abruptness has a direct signal-processing consequence through the Gabor limit [29]: widening the STFT observation window improves spectral resolution but inevitably blurs the sub-residue boundary. Because the geometric transition approximates a sub-residue step function, any window expansion beyond the minimal scale immediately introduces boundary contamination, and the monotonic decay of AUC with increasing  $\sigma$  is an empirical manifestation of this trade-off. The failure of the adaptive per-chain routing strategy to surpass the high-pass baseline further illustrates that the conflict between boundary precision and topological noise immunity operates at the residue level, not the chain level. This trade-off is a general constraint of windowed spectral analysis applied to structural boundary detection, not a limitation specific to the present method. Residue-level multi-resolution fusion or nonlinear probe combinations may partially alleviate it and remain directions for future work.

Several methodological limitations should be noted. First, the present analysis is based on X-ray crystallographic structures, which represent low-temperature or cryogenic single-conformer snapshots. Under physiological conditions, thermal fluctuations induce helix-end fraying and breathing motions [43] that would broaden the helix-coil interface; the median width of 0.145 residues should therefore be regarded as a lower bound characteristic of the crystallographic ensemble rather than a general constant. Second, the Hasimoto map encodes exclusively the  $C_\alpha$  backbone kinematics (bond-angle curvature and dihedral torsion) and is by construction blind to side-chain packing, hydrophobic interactions, and solvent effects, all of which contribute substantially to folding thermodynamics. The spectral signatures reported here thus characterize the backbone geometric component of secondary structure and do not capture the full energetic landscape. Third, the  $z$ -score linear combination used to fuse the

high-pass and low-pass probes is the simplest possible fusion strategy; nonlinear methods or locally adaptive weighting schemes may yield further improvements, though at the cost of additional free parameters. Finally, the boundary analysis relies on DSSP [1] assignments as ground truth, and DSSP itself employs a fixed hydrogen-bond energy threshold that introduces its own boundary ambiguity. Alternative assignment algorithms (e.g., STRIDE [2]) or torsion-angle clustering approaches [46] may shift individual boundary positions by one to two residues, although the statistical conclusions drawn from  $>19,000$  boundaries are unlikely to be qualitatively affected.

The static-snapshot limitation points directly to the most natural extension of this work. Because the Hasimoto map is defined at each instantaneous backbone configuration, it can be applied frame-by-frame to molecular dynamics (MD) trajectories, yielding a time-dependent effective potential  $V_{\text{re}}[n, t]$ . A joint spatial-temporal spectral decomposition of this field would enable tracking of helix-end breathing, the propagation of conformational perturbations along the backbone, and the spectral signatures of folding or allosteric transitions as they unfold in real time, building on systematic characterizations of protein family conformational diversity [47]. More broadly, the spectral entropy  $H_{\text{spec}}$  provides a sequence-agnostic, purely geometric measure of local conformational variability, complementing the graph-derived local Shannon entropy recently introduced for conformational substates in molecular dynamics [48]. High-entropy broadband regions naturally correspond to conformationally flexible segments such as hinges, loops, and intrinsically disordered regions [49] that have been associated with allosteric communication and protein-protein interactions [50]. Unlike sequence-based spectral methods that transform one-dimensional physicochemical indices into frequency repre-

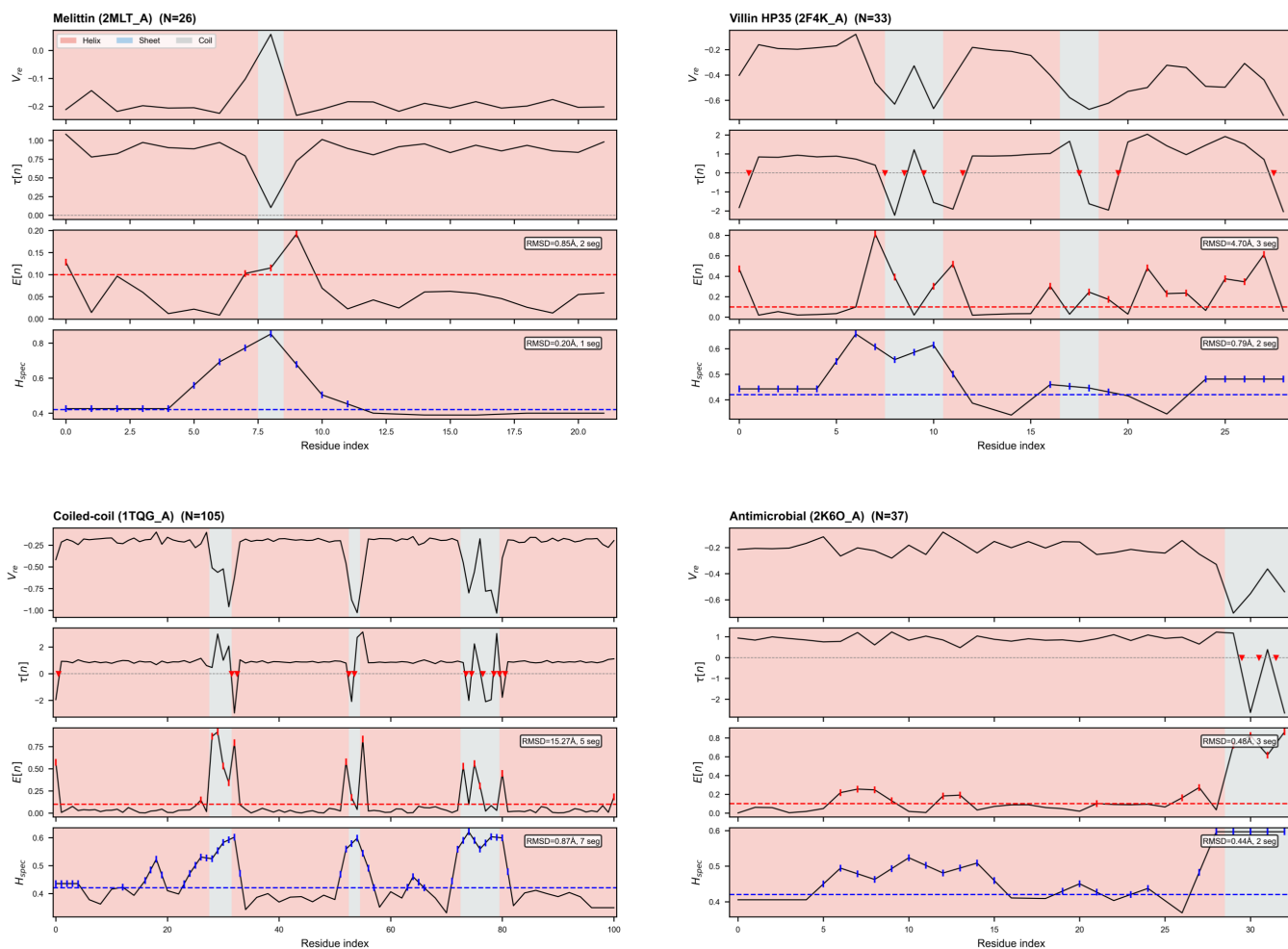


FIG. 8. Macroscopic 3D manifestation of spatial-spectral trade-offs in helical peptide reconstruction. Each panel displays the local geometric signals ( $V_{re}[n]$  and  $\tau[n]$  with sign-flip markers as red triangles) alongside the segmentation decisions made by the high-pass filter  $E[n]$  (red dashed, threshold  $\theta = 0.10$ ) and the windowed spectral entropy  $H_{spec}$  (blue dashed,  $\sigma^* = 1.5$ , optimal threshold  $\theta^* = 0.420$ ). Background shading indicates DSSP secondary structure: helix (red), sheet (blue), and coil (gray). The resulting 3D RMSD and segment counts illustrate the fundamental conflict between boundary precision and topological noise immunity. (a) Clean boundary limit (2MLT\_A): In a highly ordered peptide with no torsion noise,  $E[n]$  slightly over-segments, but both methods successfully capture the core topology (RMSD  $< 1.0$  Å). (b & c) High-pass failure and low-pass recovery (2F4K\_A and 1TQG\_A): In sequences with high-frequency geometric noise, the pointwise sensitivity of  $E[n]$  fragments the macroscopic continuous helix into disconnected segments (RMSD increases to 4.70 Å and 15.27 Å). The STFT window of  $H_{spec}$  acts as a low-pass smoother, absorbing the local defects to correctly identify the continuous DC-band structure, recovering the global topology (RMSD drops to 0.79 Å and 0.87 Å). (d) Marginal equilibrium (2K6O\_A): Both the high-pass and spectral filters achieve comparable 3D segmentation on a moderately clean helix, highlighting that structural prediction fundamentally relies on balancing these two signal-processing extremes.

sentations [22, 24, 25], the present framework operates directly on the three-dimensional differential geometry of the folded backbone, offering a complementary structural perspective. Whether this geometric spectral fingerprint can quantitatively predict functional flexibility or allosteric pathways, potentially serving as an input feature for flexibility predictors [51], remains to be validated against experimental dynamics data and larger-scale functional annotations.

In summary, this study reframes protein secondary-structure boundary detection as a signal-processing problem

subject to the Gabor spatial-spectral uncertainty principle. The sub-residue sharpness of helix–coil transitions provides independent geometric observations consistent with the high cooperativity described by the Zimm–Bragg thermodynamic model [43], and the resulting maximal-localization constraint explains both the strengths and the vulnerabilities of pointwise geometric descriptors. The dual-probe framework, combining a high-pass integrability residual with a low-pass DC energy ratio, offers a principled response to this physical trade-off and improves helix detection beyond either probe alone.

- [1] W. Kabsch and C. Sander, Dictionary of protein secondary structure: pattern recognition of hydrogen-bonded and geometrical features, *Biopolymers: Original Research on Biomolecules* **22**, 2577 (1983).
- [2] D. Frishman and P. Argos, Knowledge-based protein secondary structure assignment, *Proteins: Structure, Function, and Bioinformatics* **23**, 566 (1995).
- [3] J. Martin, G. Letellier, A. Marin, J.-F. Taly, A. G. De Brevern, and J.-F. Gibrat, Protein secondary structure assignment revisited: a detailed analysis of different assignment methods, *BMC structural biology* **5**, 17 (2005).
- [4] G. Labesse, N. Colloc'h, J. Pothier, and J.-P. Mornon, P-sea: a new efficient assignment of secondary structure from  $\alpha$  trace of proteins, *Bioinformatics* **13**, 291 (1997).
- [5] S. Khalife, T. Malliavin, and L. Liberti, Secondary structure assignment of proteins in the absence of sequence information, *Bioinformatics Advances* **1**, vbab038 (2021).
- [6] S. Rackovsky and H. Scheraga, Differential geometry and protein folding, *Accounts of Chemical Research* **17**, 209 (1984).
- [7] A. Louie, R. Somorjai, and A. Klug, Differential geometry of proteins: helical approximations, *Journal of Molecular Biology* **168**, 143 (1983).
- [8] M. Chernodub, S. Hu, and A. J. Niemi, Topological solitons and folded proteins, *Physical Review E—Statistical, Nonlinear, and Soft Matter Physics* **82**, 011916 (2010).
- [9] S. Hu, M. Lundgren, and A. J. Niemi, Discrete frenet frame, inflection point solitons, and curve visualization with applications to folded proteins, *Physical Review E—Statistical, Nonlinear, and Soft Matter Physics* **83**, 061908 (2011).
- [10] A. Krokhotin, A. J. Niemi, and X. Peng, Soliton concepts and protein structure, *Physical Review E—Statistical, Nonlinear, and Soft Matter Physics* **85**, 031906 (2012).
- [11] A. Begun, M. N. Chernodub, A. Molochkov, and A. J. Niemi, Local topology and perestroikas in protein structure and folding dynamics, *Physical Review E* **111**, 024406 (2025).
- [12] M. Prados, M. de la Torre, and F. de Soto, A frenet frame analysis of protein geometry: hints for secondary structure assignments, *arXiv preprint arXiv:2512.05660* (2025).
- [13] A. S. Davydov, Solitons and energy transfer along protein molecules, *Journal of theoretical biology* **66**, 379 (1977).
- [14] B. Rost and C. Sander, Prediction of protein secondary structure at better than 70% accuracy, *Journal of molecular biology* **232**, 584 (1993).
- [15] J. Jumper, R. Evans, A. Pritzel, T. Green, M. Figurnov, O. Ronneberger, K. Tunyasuvunakool, R. Bates, A. Žídek, A. Potapenko, *et al.*, Highly accurate protein structure prediction with alphafold, *nature* **596**, 583 (2021).
- [16] D. Eisenberg, R. M. Weiss, T. C. Terwilliger, and W. Wilcox, Hydrophobic moments and protein structure, in *Faraday Symposium of the Chemical Society*, Vol. 17 (Royal Society of Chemistry, 1982) pp. 109–120.
- [17] D. Eisenberg, R. M. Weiss, T. C. Terwilliger, The hydrophobic moment detects periodicity in protein hydrophobicity., *Proceedings of the National Academy of Sciences* **81**, 140 (1984).
- [18] J. L. Cornette, K. B. Cease, H. Margalit, J. L. Spouge, J. A. Berzofsky, and C. DeLisi, Hydrophobicity scales and computational techniques for detecting amphipathic structures in proteins, *Journal of molecular biology* **195**, 659 (1987).
- [19] W. Cheng and C. Yan, Detecting periodicity associated with the alpha-helix structure using fourier transform, *Comput. Mol. Biosci* **2012**, 109 (2012).
- [20] J. Pando, L. Sands, and S. E. Shaheen, Detection of protein secondary structures via the discrete wavelet transform, *Physical Review E—Statistical, Nonlinear, and Soft Matter Physics* **80**, 051909 (2009).
- [21] N. C. Benson and V. Daggett, Wavelet analysis of protein motion, *International journal of wavelets, multiresolution and information processing* **10**, 1250040 (2012).
- [22] V. Veljković and I. Slavić, Simple general-model pseudopotential, *Physical Review Letters* **29**, 105 (1972).
- [23] V. Veljkovic, I. Cosic, D. Lalovic, *et al.*, Is it possible to analyze dna and protein sequences by the methods of digital signal processing?, *IEEE Transactions on Biomedical Engineering* , 337 (1985).
- [24] I. Cosic, Macromolecular bioactivity: is it resonant interaction between macromolecules?-theory and applications, *IEEE Transactions on Biomedical Engineering* **41**, 1101 (2002).
- [25] Y. Wang, M. Cai, Y. Dong, Y. Ma, and K. Wei, From signal to symphony: Exploring 2d sequence representations for protein function prediction, *Journal of Chemical Information and Modeling* **65**, 12723 (2025).
- [26] H. Hasimoto, A soliton on a vortex filament, *Journal of Fluid Mechanics* **51**, 477 (1972).
- [27] Y. Wang, Structural barriers of the discrete hasimoto map applied to protein backbone geometry, *arXiv preprint arXiv:2602.13160* (2026).
- [28] Y. Wang, Piecewise integrability of the discrete hasimoto map for analytic prediction and design of helical peptides, *arXiv preprint arXiv:2602.16255* (2026).
- [29] D. Gabor, Electrical engineers-part iii: Radio and communication engineering, *Journal of the Institution of Electrical Engineers* **93**, 39 (1946).
- [30] H. M. Berman, J. Westbrook, Z. Feng, G. Gilliland, T. N. Bhat, H. Weissig, I. N. Shindyalov, and P. E. Bourne, The protein data bank, *Nucleic acids research* **28**, 235 (2000).
- [31] G. Wang and R. L. Dunbrack Jr, Pisces: a protein sequence culling server, *Bioinformatics* **19**, 1589 (2003).
- [32] R. P. Joosten, T. A. Te Beek, E. Krieger, M. L. Hekkelman, R. W. Hooft, R. Schneider, C. Sander, and G. Vriend, A series of pdb related databases for everyday needs, *Nucleic acids research* **39**, D411 (2010).
- [33] U. H. Danielsson, M. Lundgren, and A. J. Niemi, Gauge field theory of chirally folded homopolymers with applications to folded proteins, *Physical Review E—Statistical, Nonlinear, and Soft Matter Physics* **82**, 021910 (2010).
- [34] P. Virtanen, R. Gommers, T. E. Oliphant, M. Haberland, T. Reddy, D. Cournapeau, E. Burovski, P. Peterson, W. Weckesser, J. Bright, *et al.*, Scipy 1.0: fundamental algorithms for scientific computing in python, *Nature methods* **17**, 261 (2020).
- [35] E. R. DeLong, D. M. DeLong, and D. L. Clarke-Pearson, Comparing the areas under two or more correlated receiver operating characteristic curves: a nonparametric approach, *Biometrics* , 837 (1988).
- [36] H. B. Mann and D. R. Whitney, On a test of whether one of two random variables is stochastically larger than the other, *The annals of mathematical statistics* , 50 (1947).
- [37] J. Cohen, *Statistical power analysis for the behavioral sciences* (routledge, 2013).
- [38] W. J. Youden, Index for rating diagnostic tests, *Cancer* **3**, 32 (1950).

- [39] J. Lin, Divergence measures based on the shannon entropy, *IEEE Transactions on Information theory* **37**, 145 (2002).
- [40] R. Aurora and G. D. Rose, Helix capping, *Protein Science* **7**, 21 (1998).
- [41] W. H. Kruskal and W. A. Wallis, Use of ranks in one-criterion variance analysis, *Journal of the American statistical Association* **47**, 583 (1952).
- [42] N. Wiener, *Extrapolation, interpolation, and smoothing of stationary time series: with engineering applications* (The MIT press, 1949).
- [43] B. H. Zimm and J. Bragg, Theory of the phase transition between helix and random coil in polypeptide chains, *The journal of chemical physics* **31**, 526 (1959).
- [44] U. Zavrtanik, J. Lah, and S. Hadži, Backbone conformational entropy change in helix folding, *Biophysical Journal* **125**, 305 (2026).
- [45] R. López-Sánchez, M. Mompeán, and D. V. Laurents, Orientation affects hydrogen bonding cooperativity in polyproline ii helical bundles, *Communications Chemistry* **8**, 195 (2025).
- [46] V. Kannan, A comprehensive system for secondary structure analysis of protein models, arXiv preprint arXiv:2404.02909 (2024).
- [47] V. Lombard, S. Grudin, and E. Laine, Explaining conformational diversity in protein families through molecular motions, *Scientific Data* **11**, 752 (2024).
- [48] P. Senet, A. Guzzo, P. Delarue, C. Laforge, G. Maisuradze, J.-M. Heydel, F. Neiers, and A. Nicolai, Local entropy in proteins, *Chemical Science* (2026).
- [49] P. E. Wright and H. J. Dyson, Intrinsically unstructured proteins: re-assessing the protein structure-function paradigm, *Journal of molecular biology* **293**, 321 (1999).
- [50] S. A. Wankowicz and J. S. Fraser, Making sense of chaos: uncovering the mechanisms of conformational entropy, *Nature chemical biology* **21**, 623 (2025).
- [51] P. Kouba, J. Planas-Iglesias, J. Damborsky, J. Sedlar, S. Mazurenko, and J. Sivic, Learning to engineer protein flexibility, arXiv preprint arXiv:2412.18275 (2024).